

Design and Control Considerations for High-Performance Series Elastic Actuators

Nicholas Paine, *Student Member, IEEE*, Sehoon Oh, *Member, IEEE*, and Luis Sentis, *Member, IEEE*

Abstract—This paper discusses design and control of a prismatic series elastic actuator with high mechanical power output in a small and lightweight form factor. A design is introduced that pushes the performance boundary of electric series elastic actuators by using high motor voltage coupled with an efficient drivetrain to enable large continuous actuator force while retaining speed. Compact size is achieved through the use of a novel piston-style ball screw support mechanism and a concentric compliant element. Generic models for two common series elastic actuator configurations are introduced and compared. These models are then used to develop controllers for force and position tracking based on combinations of PID, model-based, and disturbance observer control structures. Finally, our actuator's performance is demonstrated through a series of experiments designed to operate the actuator at the limits of its mechanical and control capability.

Index Terms—Actuator design, force control, series elastic actuators.

I. INTRODUCTION

SERIES elastic actuation (SEA) is a departure from the traditional approach of rigid actuation commonly used in factory room automation. Unlike rigid actuators, SEAs contain an elastic element in series with the mechanical energy source. The elastic element gives SEAs several unique properties compared to rigid actuators including low mechanical output impedance, tolerance to impact loads, increased peak power output, and passive mechanical energy storage [1]–[3]. These properties align with requirements of robustness, high-power output, and energy efficiency placed on legged actuation systems. As a result, SEAs have been widely adopted in the fields of legged robotics and human orthotics [4], [5].

A. SEA Design Background

Electric SEAs contain a motor to generate mechanical power, a speed reduction to amplify motor torque, a compliant element to sense force, and a transmission mechanism to route mechanical power to the joint output. These components can be chosen and configured in many different ways, producing

designs with various tradeoffs which affect the power output, volumetric size, weight, efficiency, backdrivability, impact resistance, passive energy storage, backlash, and torque ripple of a SEA. Existing SEA designs can be analyzed to identify such tradeoffs based on their choice of speed reduction, compliant element, and transmission mechanism.

In [6]–[9], the authors propose rotary designs based primarily on commercially available off-the-shelf components, using a planetary gearbox for the speed reduction, rotary or compression springs as the compliant element, and power transmission through a bevel gear [8] or chain/cable [6], [7]. Use of off-the-shelf parts make these designs relatively low cost and easy to implement. However, multistage planetary gearboxes have poor efficiency (60–70% for three-stage) and can be difficult to backdrive. Additionally, gear teeth introduce torque ripple and backlash and are easily damaged by impact loads. Bevel gears compound these effects by adding additional backlash and loss due to friction.

A compact rotary SEA design can be achieved using a harmonic drive and a high-stiffness planar spring [10], [11]. Hutter *et al.* [12] also use a harmonic drive but chooses lower stiffness die/compression springs. Harmonic drives benefit from having no backlash and being small in size but suffer from poor efficiency (60–75% depending on ratio, speed, and lubricant), poor backdrivability, torque ripple, and are more expensive than planetary/spur gears. The high-stiffness planar springs of [10] and [11] deflect only a small amount under load and, therefore, store less energy than designs with softer springs. Conversely, stiff springs increase an actuator's open-loop bandwidth which may be desirable for applications with high force bandwidth requirements.

In [12] and [13], the authors use linear springs coupled to rotary shafts and place the springs between the motor and the chassis ground to achieve compact actuator packaging with low spring stiffness.

In [14] and [15], the authors place the spring within the reduction phase. This arrangement reduces the torque requirement on the spring compared to designs with the spring at the actuator output. A spring's wire gauge is directly correlated with the amount of torque it can safely support, which allows the spring in these designs to be smaller. However, because the torque compressing the spring is reduced, the energy stored in the spring is reduced as well. Kong *et al.* [14] use a novel worm-gear/rotary-spring/spur-gear design which allows an orthogonal placement of the motor relative to the joint axis at the cost of reduced efficiency and nonbackdrivability due to the worm gear. Taylor [15] uses two motors in parallel and has a relatively small reduction through a series of gears and a cable transmission. Two motors in

Manuscript received June 21, 2012; revised October 10, 2012, January 23, 2013, and June 10, 2013; accepted June 10, 2013. Date of publication July 9, 2013; date of current version April 11, 2014. Recommended by Technical Editor S. C. Mukhopadhyay.

N. Paine is with the Department of Electrical and Computer Engineering, University of Texas at Austin, Austin, TX 78712 USA (e-mail: npaine@utexas.edu).

S. Oh and L. Sentis are with the Department of Mechanical Engineering, University of Texas at Austin, Austin, TX 78712 USA (e-mail: sehoon74@gmail.com; lsentis@austin.utexas.edu).

Color versions of one or more of the figures in this paper are available online at <http://ieeexplore.ieee.org>.

Digital Object Identifier 10.1109/TMECH.2013.2270435

parallel effectively doubles the continuous motor torque which allows use of a small speed reduction for the high actuator output speed. This is achieved at the cost of increased weight and complexity and is difficult to implement with brushless direct current (BLDC) motors due to commutation synchronization issues.

In [16]–[18], the authors propose prismatic designs which use ball screws as the primary reduction mechanism followed by a cable drive to remotely drive a revolute joint. Ball screws are highly efficient, even for large speed reductions (85–90%), are backdrivable, are tolerant to impact loads, and do not introduce torque ripple. However, designs based on ball screws have not achieved the levels of compactness seen in the rotary actuator design. Edsinger-Gonzales and Weber [16] include a belt drive between the motor and the ball screw which enables an additional speed reduction due to the pulley diameter ratio.

Pratt and Krupp [19] use a ball screw speed reduction and removes the need for a cable transmission by directly driving the joint output with a pushrod mechanism.

Variable stiffness actuators extend the SEA concept by adding an additional degree of freedom which is capable of mechanically adjusting the passive elastic stiffness [20]–[24]. Other SEA implementations have experimented with nonlinear spring stretching to maximize energy storage [25].

B. SEA Control Background

Many different architectures have been proposed for controlling series elastic actuators. Some of the variation in controller design is rooted in differences imposed by the hardware. For example, force can be observed either by measuring change in resistance, as is accomplished using strain gauges in [1], or by measuring spring deflection and applying Hooke's law, as shown in [26]. A control strategy for hardware designs using spring deflection sensors may treat a motor as a velocity source, and transform desired spring forces into desired spring deflections. However, for hardware designs using strain gauges, the force sensor does not output an intermediate displacement value, but maps change in resistance directly to applied force. For such a system, modeling the motor as a force source is more convenient.

Further classification of SEA control strategies may be made based on the types and combinations of control structures used. [9], [27], [28] measure the spring force and control motor force using some subset of PID control structures (P, PD, etc.). If friction and backlash are too large, then a pure high-gain PID approach can suffer from stability issues. To remedy this issue, Pratt *et al.* [29] suggest using position feedback as the innermost control structure for force control. This idea has been adopted and carried on by many others, treating force control as a position or velocity tracking problem [10], [25], [30], [31]. Another class of controllers use PID control but also consider the dynamics of the mechanical system to improve the frequency response of force control [1], [20]. In [8], [14] the authors use PID, model-based, and disturbance observer (DOB) structures together to achieve impressive torque tracking performance. In this paper, we build upon the force controller presented in [8] by proposing a simple method for obtaining the closed-loop model used by the DOB.

C. Actuator Performance

In this paper, we define actuator performance by a combination of metrics which include measured power-to-weight ratio, force tracking accuracy and bandwidth, position tracking accuracy and bandwidth, and actuation efficiency.

These metrics are heavily influenced by decisions made at the design phase. For example, heat is generated when torque is produced by an electric motor. Therefore, the continuous power output of an electric actuator directly depends on the motor's thermal properties. However, a motor is able to generate torques greater than the thermally permissible continuous limit if done so for short periods of time. These intermittent torques often far exceed those which the speed reduction mechanism can support. Because of this discrepancy, the speed reduction mechanism is commonly the component which determines the peak output power capability of an actuator, not the motor. Additionally, the speed reduction mechanism is often a large source of loss in an electric actuator, so its selection critically influences efficiency as well.

For actuators with a fixed range of motion, the performance metrics also depend on actuator control strategies. Actuator power output is maximized when applying large torques at high velocities. Obtaining high velocities within a fixed range of motion requires short bursts of acceleration to and from rest. This requirement differs from those of continuous travel actuation schemes, whose maximum power output may be achieved simply with a viscous load and a step or ramp in the desired torque. For actuators with a fixed range of motion, the boundary conditions placed on high-power experiments necessitate the use of automatic control strategies to ensure the actuator operates within its permissible range of motion. It is then the combined performance of the hardware design and the control design which determines usable power-to-weight ratio of the actuator.

Detailed data on these performance metrics are not currently publicly available for most existing electric SEAs. Pestana *et al.* [4] provide experimental data for the actuator described in [19] which achieves 64 W/kg. Hutter *et al.* [32] provide the power exerted during a hop for the knee joint of [12] (close to 60 W), but because the actuators are integrated into a three degree-of-freedom leg, the actuator power-to-weight ratio is difficult to calculate.

D. Contributions and Paper Structure

This paper highlights research in development of the University of Texas Series Elastic Actuator (UT-SEA), a compact, lightweight, high-power electric actuator (see Fig. 1). Our contributions include: 1) a novel mechanical design that is more compact and lightweight than previous ball screw SEA designs; 2) a study of the theoretical limitations imposed by the dynamics of two common SEA design configurations; 3) an improvement in the controller design and implementation methodology for force and position control of SEAs; and 4) achievement of leading experimental results in the field of electric SEA performance (94 W/kg, 77% mechanical efficiency) which we believe may

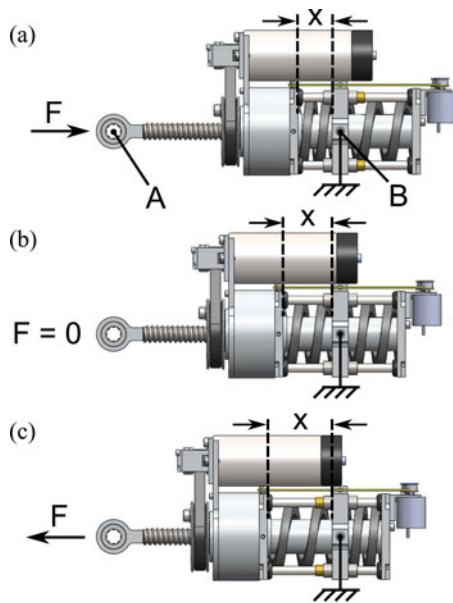


Fig. 1. UT-SEA operation for a fixed-displacement variable-force scenario. Actuator displacement is defined as the distance between points A and B. This distance remains constant while spring deflection (x) depends on actuator force.

serve as a performance benchmark for other fixed-range-of-motion, passively cooled, high force electric actuators.

We first describe the design motivation behind the electrical power system and motor operation, followed by explanation of the actuator drivetrain and mechanical design. We then generalize our discussion to generic models for SEAs which are used to build controllers for actuator force and position. Finally, we validate the entire system in hardware through a series of experiments demonstrating actuator speed, power, and efficiency.

II. DESIGN

Nature provides many examples of well-designed actuators. An average human adult male can produce 1500 W of mechanical power during pedaling exercises, which corresponds to a whole-body power-to-weight ratio of 19.5 W/kg [33]. To achieve similar performance in man-made machines, great care must be taken during the actuator design phase to maximize mechanical power output while keeping actuator size and weight small. Excess actuator weight reduces a robot's whole-body power-to-weight ratio while large size limits a modular actuator's applicability in dense high-degree-of-freedom robot designs. Hydraulic actuation is one approach which achieves these goals but suffers from inefficient operation as discussed in [34].

We began the design process with a set of loose performance specifications for a robotic knee actuator (peak joint torques of 70 N·m and maximum velocities of 15 rad/s). These specifications were obtained from simulations of legged locomotion of a 15-kg robot in rough terrain. However, it is important to note that the design goal of this particular actuator was not for use in any specific robot, only for the experimental study of its mechanical power output.

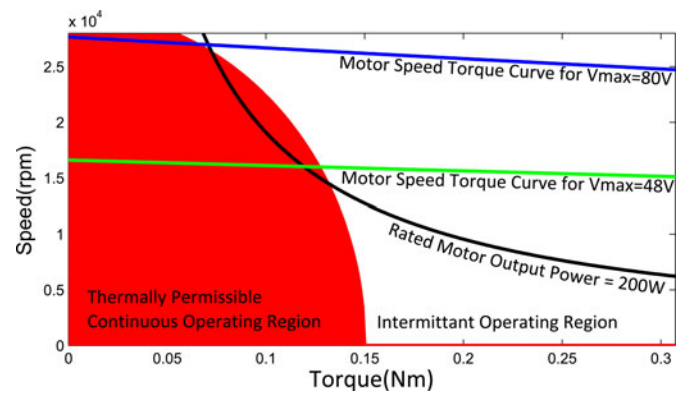


Fig. 2. Motor operating range for Maxon EC-powermax 30 as taken from the datasheet. A motor is capable of operating inside of the area below the speed–torque curve for a given applied voltage. Increasing voltage to 80 V greatly increases the operating range of the motor, particularly in the continuous operating region.

A. Motor

The motor in an electric actuator is the source of mechanical energy and, therefore, must be chosen and integrated carefully to achieve optimal performance. Motors convert electrical voltage and current into mechanical velocity and torque. The higher the applied voltage, the greater the obtainable velocities and torques become. All motor windings have electrical resistance, which produce heat when current flows through them. Because motor torque is proportional to winding current, motor torque is limited by the heat generated in its windings. High temperatures can damage the motor by depolarizing magnets, melting bonding agents, or damaging windings, if brought above certain manufacturer-supplied values.

A pulse-width-modulated (PWM) signal is used to efficiently modulate the voltage applied to the motor. Due to the resistor–inductor (RL) circuit behavior of the motor windings, their current response to the PWM voltage signal takes the shape of a first-order exponential signal which rises when the PWM signal is high and falls when the PWM signal is low. The maximum absolute value of this transient current signal depends on 1) PWM frequency (how long the signal has to rise or fall); 2) the L/R time constant of the motor circuit; and 3) the amplitude of the PWM signal, which corresponds to the voltage used to drive the motor (bus voltage). If the maximum absolute value of the transient current is too large, motor heating will occur simply due to the PWM signal without any useful motor torque being produced.

High bus voltage is desirable to maximize the achievable motor velocity and torque. Motor manufacturers typically provide a “rated voltage” for each motor which keeps the transient motor current within reasonable values for common PWM frequencies (10–20 kHz). However, larger voltage and thus greater mechanical power is possible as long as the transient current is limited. For the UT-SEA, we chose a Maxon EC-powermax 30 BLDC motor with a rated voltage of 48 V. To increase mechanical power output, we instead supply the motor with 80 V (see Fig. 2). The transient motor current is regulated by using a 32-kHz PWM servo drive (Elmo Ocarina 15/100) and by adding high-current

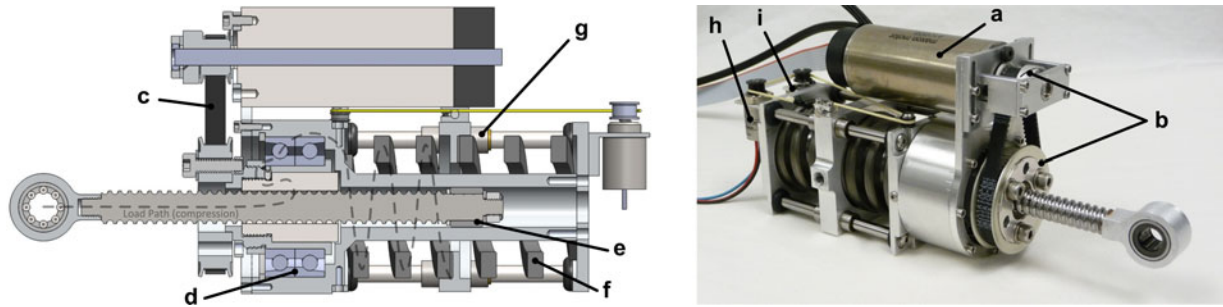


Fig. 3. Cross section of the UT-SEA showing drivetrain components including (a) Maxon EC-4pole 30 200W BLDC motor, (b) 3:1 pulley speed reduction, (c) low backlash timing belt, (d) angular contact bearings, (e) piston-style ball screw support, (f) high compliance springs, (g) miniature ball bearing guides, (h) absolute encoder, and (i) incremental encoder. The compression load path is depicted as well.

inductors in series with the motor. Calculations provided by the drive manufacturer indicated that a series inductance of 0.082 mH would keep the transient current within reasonable values. The small added mass of the inductors is justified in that they allow the continuous force of the actuator to be increased by 66% without sacrificing the output speed.

The high motor speed produced by high bus voltage enables the use of a large speed reduction which increases both the intermittent and continuous torque capability compared to designs with lower voltages and lower speed reductions. For this motor, the gain in the output power by using 80 V compared to 48 V is less pronounced due to the diminished continuous torque at very high motor speed. The final motor output characteristics indicated that a design using a speed reduction of approximately 175:1 would allow the actuator to meet the specified torque and speed requirements.

B. Drivetrain

To maximize mechanical power at the joint, energy must be transmitted from the motor to the joint with as few losses as possible. We chose a pulley/ball-screw speed reduction design similar to [16] for several reasons. A pulley/ball-screw reduction is efficient (typically above 90%), impact resistant, and back-drivable, while the pulley ratio reduces the high motor speed to a speed more suitable for driving the ball screw.

Unlike [16] and other ball screw SEA designs, our design drives the ball nut instead of the ball screw (P. Garrec [35] uses a similar ball-nut-driven design but is a nonseries-elastic cable-driven actuator). Driving the ball nut enables two key features which reduce the size and weight of the UT-SEA. First, ball screw support is incorporated directly into the actuator housing using an innovative piston-style guide (see Fig. 3). This feature replaces the long, bulky rails used to support the output carriage in conventional prismatic SEA designs. Second, the compliant element is placed concentrically around the piston-style ball screw support which gives series elasticity without adding to the length of the actuator. These two features combine together to define the compact form factor of the UT-SEA.

The ball nut is supported by dual angular contact bearings which allow the ball nut to rotate within the housing while transmitting axial force from the ball nut to the housing. Custom preloaded die springs (manufactured by Diamond Wire Spring

Co.) transmit force from the actuator housing to the chassis ground. The die springs are supported by four miniature ball bearing guide rails (Misumi) which are mounted to the housing using grommets that allow for slight misalignment during operation. The miniature ball bearing guides offer both lower friction and higher tolerance to torsional loads than bushing style guides. Force is sensed using a 20 000 count-per-revolution incremental encoder (Avago AEDA 3300) along with an absolute sensor (Novotechnik Vert-X 1302) to remove the need for startup calibration. A low stretch, low creep Vectran cable is attached to the chassis ground and is routed around the two spring deflection sensors using pulleys and an idler. Overall actuator position is measured combining readings from the motor encoder and the spring encoders. An absolute rotary sensor on the driven joint is used to initialize actuator position.

C. Spring Placement and Stiffness

There are two common arrangements of components found in SEA designs. The first arrangement, which we will refer to in this paper as a force sensing series elastic actuator (FSEA), places the compliant element between the gearbox output and the load. The second arrangement, which we will refer to as a reaction force sensing series elastic actuator (RFSEA), places the spring between the motor housing and the chassis ground.

From a design standpoint, there are several tradeoffs between the two arrangements. RFSEA style actuators have the advantage of being more compact since the compliant element does not have to travel with the load but may be placed statically behind the actuator (or it can be remotely located as shown in [12] and [13]). Prismatic RFSEAs also have greater range of motion for a given ball screw travel length compared to prismatic FSEAs as shown in Fig. 4. The primary drawbacks of RFSEAs are less direct force sensing, reduced force tracking performance, and decreased protection from impact loads as described in Section III-B. An RFSEA style design was chosen to minimize the bounding volume of the UT-SEA. However, this design decision was heavily influenced by the selection of the pushrod/ball-screw drivetrain. The drivetrain exhibited strong radial symmetry and possessed long, narrow ball screw support structure which allowed die springs to be integrated without excess bulk. Additionally, the decreased protection from impact loads of an RFSEA design is somewhat, though not completely,

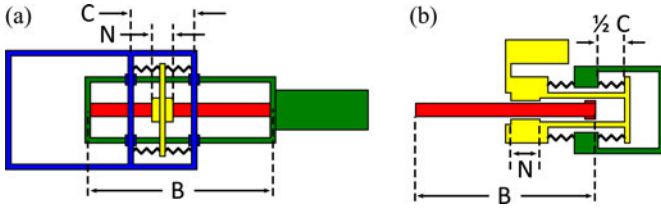


Fig. 4. Range of motion comparison between prismatic (a) FSEAs and (b) RFSEAs. For simplification, we assume that springs are fully compressible, spring plates have zero thickness, and the FSEA carriage travel is constrained to the length of the ball screw. The notations represent B: ball screw length, C: carriage length, N: ball nut length. Range of motion is then $B - C$ for the FSEA and $B + C - N$ for the RFSEA.

TABLE I
UT-SEA SPECIFICATIONS

UT-SEA Design Specifications		
Weight	1168 g	2.575 lbs
Stroke	6 cm	2.36 in
Max Speed	32.5 cm/sec	12.79 in/sec
Continuous Force	848 N	190 lbs
Intermittent Force	2800 N	629 lbs
Spring Stiffness	278 N/mm	1587 lbs/in
Force Resolution	0.31 N	0.069 lbs
Operating Voltage	80V	

mitigated by the impact tolerance of the ball screw drivetrain in the UT-SEA.

Spring stiffness for the UT-SEA was chosen to maximize energy storage. For a given force, soft springs are able to store more energy than stiff springs. Peak force, desired deflection (maximum possible deflection to minimize stiffness), and the geometric constraints of the actuator were given as design specifications to Diamond Wire Spring Co. They then designed and manufactured a spring with a stiffness rate of 138 N/mm which effectively doubles to 277 N/mm for the actuator spring constant because two springs are used with precompression.

D. Design Summary

The end result of the design process is a pushrod RFSEA-style actuator that is compact and modular enough to be integrated into dense mechanical designs. Rotary joint designs using linear actuators can benefit from the nonlinear linkage kinematics created at the joint at the cost of a fixed range of motion (refer to Fig. 12). The torque generated by such a linkage has an angle-dependent moment arm which can be used to provide high torque and high speed capability where they are needed. A summary of the design parameters for the UT-SEA can be seen in Table I.

III. MODELING AND CONTROL

This paper discusses two main control objectives for the UT-SEA. First, when operated in a force control mode, the UT-SEA should be capable of closely approximating an ideal force source. An ideal force source is able to accurately track a desired force signal both in steady state and for higher band-

width, rapidly changing desired force signals. An ideal force source is the common building block for several higher level control strategies, including: operational space control [36], virtual model control [37], impedance control [38], and classical model-based control, among others. In this paper, we only consider classical model-based position control as an extension to a near-ideal force source. We create this near-ideal force source by developing a force control strategy which attempts to minimize measured force error by sending desired current commands to the motor servo drive.

The second control objective discussed in this paper is stable and accurate tracking of joint position for high joint velocities. As discussed in Section I-C, this objective is made difficult due to the fixed-range-of-motion requirement and, therefore, requires accurate tracking of large accelerations. We achieve this objective using a model-based control strategy which relies on the near-ideal force source developed for the first control objective.

Because both the control objectives require excellent dynamic response, it is essential to understand the basic dynamics of the UT-SEA. We begin discussion of the controller development process by defining a simple model of the UT-SEA. This model is generic and may be applied to other RFSEA style actuators. In parallel, we also present an FSEA actuator model and compare it against the RFSEA model to understand the inherent differences between the two SEA arrangements. Then, using the RFSEA model, we develop force and position controllers for the UT-SEA.

A. Modeling

Fig. 5 shows simple models for both the FSEA and RFSEA style actuators. In the FSEA model [see Fig. 5(c)], generalized motor force (F_m) is generated between chassis ground and a lumped sprung mass (m_k) which includes rotor inertia, the gearbox reduction, and transmission inertia. If the motor is unpowered and backdriven, a viscous backdriving friction (b_b) is felt from transmission friction and motor friction. The spring is between the transmission output and output mass (m_o) and has stiffness (k) and viscous friction (b_k) generated by the spring support mechanism. In the RFSEA model, the spring and force generating elements are switched. In addition, the distribution of sprung mass and output mass is different for an RFSEA. m_o in the RFSEA model includes rotor inertia, the gearbox reduction, and transmission inertia. m_k varies by the design. For the UT-SEA, m_k includes the mass of the actuator housing and motor, including the rotor mass.

A high-output impedance model is useful for simplifying the force controller design problem [see Fig. 5(d)]. It assumes that the actuator output is rigidly connected to an infinite mass, which cannot be moved. For the high-output impedance models, the sprung mass feels a summation of forces from 1) the motor (F_m); 2) the spring (F_k); 3) lumped viscous friction ($F_{b_{eff}}$) where $b_{eff} = b_b + b_k$; and 4) from other disturbances that are difficult to model (F_d) such as the torque ripple from commutation, the torque ripple from the gearbox due to teeth engaging and disengaging, backlash, and various forms of friction such as stiction, and coulomb friction.

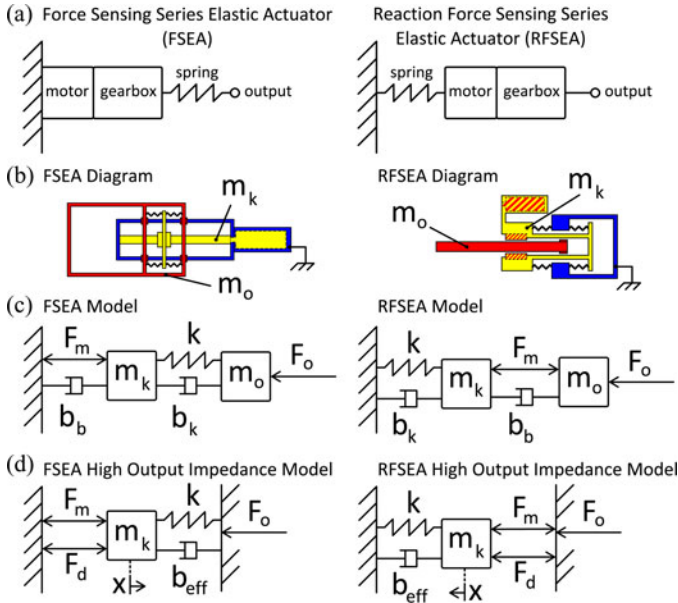


Fig. 5. Models for FSEA and RFSEA style actuators. The notations represent: F_m : motor force, F_o : output force, b_b : viscous backdriving friction, b_k : viscous spring friction, k : spring constant, x : spring deflection, m_k : lumped sprung mass, m_o : output mass, b_{eff} : lumped damping which equals $b_b + b_k$, and F_d : disturbance forces and forces which are difficult to model.

B. FSEAs Versus RFSEAs

The force sensing challenge is to calculate force felt at the actuator output (F_o) given measurement of spring deflection (x). For both the FSEAs and RFSEAs, the spring acts as the force sensor. The difference between the two is where the spring is located relative to the output force. This discrepancy does not affect low-frequency force measurement but must be taken into account to measure high-frequency forces accurately.

For FSEAs with high output impedance [see Fig. 5(d)], $F_o = F_k + F_{b_{eff}}$. If $F_{b_{eff}}$ is small, which can be accomplished with careful mechanical design, then F_o can be closely approximated by measuring F_k alone. This simplification removes the need to measure or calculate time derivatives of x :

$$F_{FSEA} = F_k = kx. \quad (1)$$

For RFSEAs with high output impedance, $F_o = F_m + F_d = F_{m_k} + F_{b_{eff}} + F_k$. Here, measurement or calculation of time derivatives of x is critical in considering the large forces of F_{m_k} and $F_{b_{eff}}$. The output force can be observed as follows:

$$F_{RFSEA} = F_{m_k} + F_{b_{eff}} + F_k = m_k \ddot{x} + b_{eff} \dot{x} + kx. \quad (2)$$

These equations tell us that force sensing for the RFSEA style actuators should possess models of sprung mass and viscous damping and should be able to measure or calculate both \dot{x} and \ddot{x} for accurate force sensing across the frequency spectrum.

An additional drawback of RFSEAs is revealed when considering internal forces required to generate a desired output force. For an FSEA, the relationship between F_k and F_o is given by

$$\frac{F_k(s)}{F_o(s)} = \frac{k}{sb_{eff} + k} \quad (3)$$

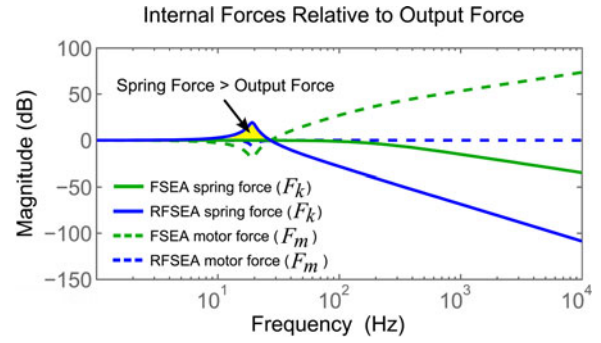


Fig. 6. Relation of internal actuator forces to output force. The four lines represent equations (3), (4), (5), and (6). As the figure shows, RFSEA spring force exceeds output force for resonant frequencies. Parameters are selected to match the UT-SEA design.

where as for a RFSEA, the same relationship is given by

$$\frac{F_k(s)}{F_o(s)} = \frac{k}{s^2 m_k + sb_{eff} + k}. \quad (4)$$

Similarly, the relations between F_m and F_o for FSEAs (5) and RFSEAs (6) are as follows:

$$\frac{F_m(s)}{F_o(s)} = \frac{s^2 m_k + sb_{eff} + k}{sb_{eff} + k} \quad (5)$$

$$\frac{F_m(s)}{F_o(s)} = \frac{s^2 m_k + sb_{eff} + k}{s^2 m_k + s(b_{eff} + b_b) + k}. \quad (6)$$

Plotting the frequency response of (3), (4), (5), and (6) yields the results shown in Fig. 6. Each line represents an internal force relative to the actuator output force across the frequency spectrum. A magnitude greater than one (0 dB) indicates that, at the represented frequency, the internal force value is greater than the output force. The motor force for both the FSEA and RFSEA remains less than or equal to the output force below the resonant frequency. The motor force for the FSEA increases for the frequencies greater than the resonant frequency because the motor force must counteract the low-pass filter created by the mass-spring system. The RFSEA is able to produce high-frequency forces without an increased burden to the motor force. The problem regarding the RFSEA design lies in the spring force, which is the only internal force to increase above output force for resonant frequencies and below. The resonant peak for spring force is about 15 dB (a factor of around 5) for the UT-SEA, meaning the spring force is five times greater than the output force. The mechanical design of UT-SEA assumes peak forces occur at the output, meaning large forces from resonance could easily result in mechanical failure. We address this issue with our force control strategy by choosing to regulate the spring force rather than the output force.

The following points summarize key differences between FSEAs and RFSEAs.

- 1) Accurate force sensing for RFSEAs requires knowledge of k , b_{eff} , m_k , x , \dot{x} , and \ddot{x} , where as FSEAs only require k and x for a close approximation of the output force.
- 2) FSEA output force can safely track a reference force signal up to and past resonant frequencies but will require large

motor effort at high frequencies. RFSEAs cannot safely track references force signals close to their resonant frequencies due to large resonant spring forces, but can track high-frequency force signals with low motor effort.

- 3) FSEAs place a mechanical low-pass filter between the output and the gearbox, making them more tolerant to impact forces than RFSEAs.

Based on these observations, FSEAs are better suited for force control applications. However, as discussed in Section II-C, the excellent size and packaging characteristics of RFSEAs outweigh the tradeoffs in force controllability for our application and this configuration was, therefore, chosen for the UT-SEA. Accurate force sensing is achieved in our implementation by using high-precision encoder data processed with a standard model-based infinite impulse response filter.

C. Force Control

Our proposed force controller uses a structure similar to [8] but differs in that the DOB is not designed based on an analytical model of the inner PID control loop, but is designed using a model obtained from experimental system identification. In this section, we provide a simplified explanation of the force control structure, and describe the system identification process used to obtain the model used in the DOB.

The goal of force control is to make the measured actuator output force (F_o) track a desired force profile (F_d) using motor current (i_m) as the plant input and spring deflection (x) as the output. However, as discussed in Section III-B, because the UT-SEA is an RFSEA style actuator F_o cannot safely track F_d for all frequencies. Instead, our force control approach regulates spring force (F_k). This decision sacrifices force tracking of F_o near resonant frequencies but guarantees safe and oscillation free force tracking at all frequencies. Additionally, because F_k is the control target, this approach applies equally to both FSEA and RFSEA designs. The effects of this decision on the tracking accuracy of F_o will be shown later in this paper (see Fig. 11 for frequency response and Fig. 15 for time domain response).

For a given output force, the motor current required to produce this force can be approximately calculated with knowledge of the motor torque constant (k_τ), actuator speed reduction (N_{bs}), and drivetrain efficiency (η). For the UT-SEA, the mapping from the motor torque (τ) to the ball screw force (F) results from a pulley reduction (N_p) and a ball screw, which is parameterized by ball screw lead (l)

$$N_{bs} = \frac{F}{\tau} = \frac{2\pi N_p}{l}. \quad (7)$$

The inverse of N_{bs} , η , and k_τ can be used as a feedforward term in a force control scheme (see Fig. 7).

Without feedback compensation, unmodeled actuator friction will reduce force tracking accuracy. A PID compensator ($K_p = 0.072$, $K_i = 0$, $K_d = 0$) addresses this problem by producing control effort as a function of measured force error $e = F_d - kx$, where kx represents the measured force as calculated using Hooke's Law.

Due to stability limitations, PID gains can only be increased up to certain values. To improve the force tracking performance

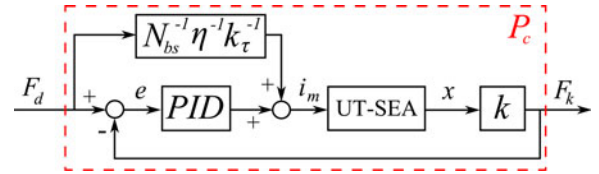


Fig. 7. PID force controller used for closed-loop system identification. The physical actuator is denoted by the “UT-SEA” block, which takes an input of motor current and produces spring deflection as an observable output. The notations represent N_{bs} : ball screw speed reduction, η : drivetrain efficiency, k_τ : motor torque constant, k : spring constant, and P_c : the closed-loop transfer function from F_d to F_k .

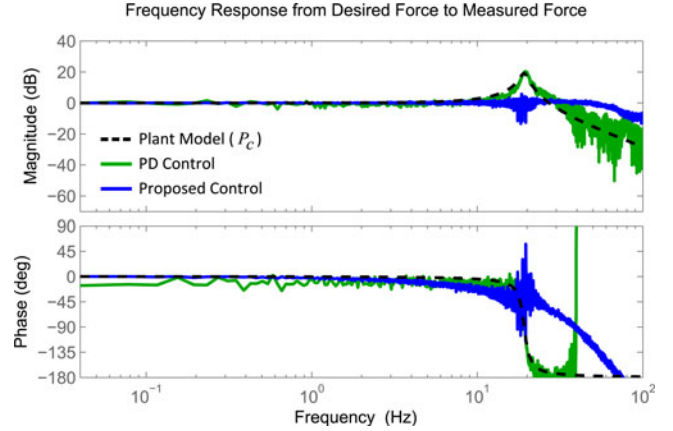


Fig. 8. Measured frequency response of two force control strategies. The proposed controller (see Fig. 9) improves upon PD control (see Fig. 7) by 1) removing the resonant peak (occurring at 19.2 Hz); 2) increasing bandwidth to 60 Hz; and 3) reducing force tracking error (see Fig. 10).

further and to remove steady-state error another control approach is required. As demonstrated by [39], a DOB may be used to 1) measure and compensate for error from disturbances; and 2) reduce the effect of plant modeling error. To use a DOB, a nominal plant model is required. For this application, the DOB plant is the closed-loop transfer function (P_c) created by the PID controller shown in Fig. 7. To obtain an accurate representation of P_c , we implement the controller shown in Fig. 7 in hardware, fix the actuator output (m_o) to ground to match the high output impedance model of Fig. 5(d), and perform system identification of P_c using an exponential chirp signal for F_d . Plotting the frequency response of the magnitude and phase of F_k/F_d (see Fig. 8) identifies a second-order system, which we model as the mass-spring-damper of Fig. 5(d). With k measured before the actuator is assembled, the only unknowns are the sprung mass and effective damping. Fitting the mass-spring-damper model to the experimental data results in $m_k = 18$ kg and $b_{eff} = 250$ N·s/m and a damped resonant frequency of 19.2 Hz. This model is shown as the dashed line in Fig. 8

$$P_c = \frac{F_k(s)}{F_d(s)} = \frac{k}{s^2 m_k + s b_{eff} + k}. \quad (8)$$

With the nominal DOB plant model identified, the DOB is incorporated into the force controller as shown in Fig. 9. Measuring the frequency response of the controller with the DOB added shows improved tracking performance compared

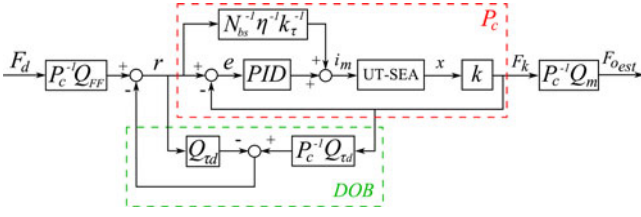


Fig. 9. Block diagram of the proposed force control structure. The physical actuator is denoted by the “UT-SEA” block. The Q functions are low-pass filters defined by (9).

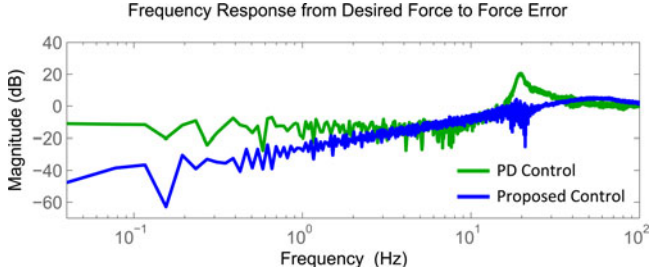


Fig. 10. Measured force tracking error versus frequency for two force control strategies. The proposed control technique reduces error at low frequencies by 98.4% (36 dB) compared to PD control.

to PD control (see Fig. 8). In fact, low-frequency force tracking error is reduced 98.4% by adding the DOB to the PD controller (see Fig. 10). The DOB forces the closed-loop response to fit closely to the mass–spring–damper model. The DOB includes a filter ($Q_{\tau d}$) which is required to make the inverse plant model realizable and to attenuate high-frequency disturbances. $Q_{\tau d}$, with the rest of the Q functions depicted in Figs. 9 and 13, is implemented as a low-pass Butterworth filter and has the following transfer function:

$$Q(s) = \frac{1}{(s/\omega_c)^2 + 1.4142(s/\omega_c) + 1}. \quad (9)$$

The cutoff frequency of each filter (ω_c) was determined empirically ($Q_{\tau d} = 60$ Hz, $Q_{FF} = 20$ Hz, $Q_m = 20$ Hz) and in general should be set higher than the desired closed-loop control bandwidth of the application. For a more detailed description on Q filter design and for discussions on controller stability, refer to [8] and [14].

Ideally, the magnitude of the closed-loop transfer function of the force controller should be close to one (0 dB) over some desired bandwidth. As can be seen in Fig. 8, the PD controller amplifies the spring force by 20 dB (a factor of 10) for excitation signals close to the resonant frequency. To remove this resonance, a feedforward filter is introduced which is created using the inverse nominal plant dynamics (P_c^{-1} in Fig. 9). A low-pass filter (Q_{FF}) is again used to make the inverse transfer function realizable. Finally, although it is not used in the force feedback loop, a filter is used to generate an estimate of output force (F_{o_est}) from spring deflection measurement ($P_c^{-1}Q_m$ in Fig. 9) which is used for observation purposes. A comparison between tracking performance of F_k and F_{o_est} is shown in Fig. 11. The dip in the F_{o_est} signal around the resonant frequency

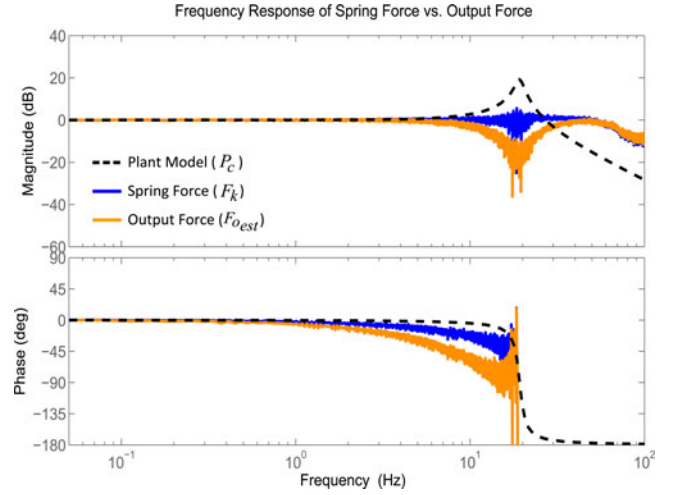


Fig. 11. Closed-loop force tracking performance of spring force (F_k) and estimated output force (F_{o_est}) for the UT-SEA.

is intentional and maintains F_k below F_d to ensure structural integrity of the actuator.

D. Position Control

In this section, we develop a position controller which builds upon the force controller. However, for position control, we no longer assume that the actuator is in a high-impedance configuration. While moving from a high-impedance configuration changes the plant of the force controller, experimental tests of the position controller show high tracking accuracy and large bandwidth. We believe there are three reasons why this is the case: 1) Output inertia is coupled to the motor rotor inertia through a large speed reduction (175:1 at $\theta_a = 90^\circ$) which reduces the inertia seen at the motor by the square of the reduction. This significantly reduces the effect of load inertia on the resonant frequencies of the actuator. 2) The force control DOB is designed to reduce the sensitivity of the controller to modeling error. Any change in the plant that occurs from the reduced output impedance is attenuated by the DOB. 3) The combined effects of 1) and 2) help maintain the effectiveness of the feed-forward inverse dynamics block of the force controller so that actuator resonance is suppressed. The small force error that does develop in Section IV can be attributed to this difference in the plant model.

By using the aforementioned force controller as the innermost component of the position controller, we are able to treat the actuator as a nearly ideal force source. This force source generates a torque through a mechanical linkage with a moment arm (L) as depicted in Fig. 12. The actuator force (F) generates an arm torque (τ_a) depending on the arm angle (θ_a) according to the following equation:

$$\tau_a = FL(\theta_a) = F \frac{cb \sin \theta_a}{\sqrt{b^2 + c^2 - 2bc \cos \theta_a}}. \quad (10)$$

The dynamics relating τ_a to θ_a with arm inertia (J_a) and joint friction (B_a) are

$$\tau_a = J_a \ddot{\theta}_a + B_a \dot{\theta}_a + \tau_g(\theta_a) \quad (11)$$

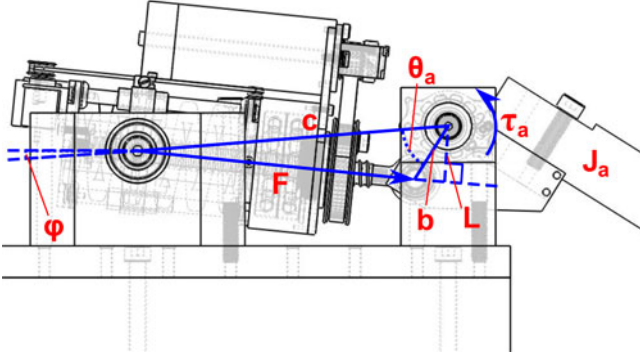


Fig. 12. UT-SEA mounted on a test bench with the prismatic linkage geometry shown. The notations represent: L : linkage moment arm, c : distance between the actuator pivot and the arm pivot, b : distance between the arm pivot and the pushrod pivot, F : actuator force, τ_a : torque exerted on the output arm, θ_a : output arm angle, J_a : inertia of the output arm, ϕ : offset angle. Values used during testing of the actuator are: $b = 0.025$ [m], $c = 0.125$ [m]. Speed reduction from motor output to arm output is 175:1 at $\theta_a = 90^\circ$.

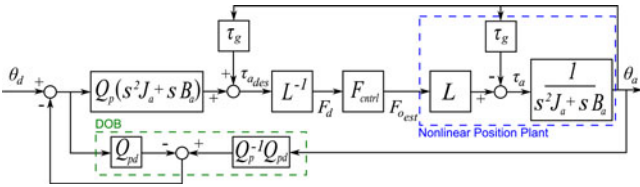


Fig. 13. Block diagram of the control structure used for position control. The notations represent: τ_g : gravity compensation torque, L : nonlinear linkage kinematics, F_{ctrl} : the force control block shown in Fig. 9. The Q functions are low-pass filters defined by (9).

where τ_g is the torque due to gravity and is parameterized by the mass of the output link (m_a), the distance from the point of rotation to the center of mass (l_m) and an angle (ϕ) to correct for c in Fig. 12 not being orthogonal to the gravity vector

$$\tau_g(\theta_a) = -m_a g l_m \cos(\theta_a + \phi). \quad (12)$$

Combining (10), (11), and (12), the full dynamics from F to θ_a are then represented by the following nonlinear differential equation:

$$F = \frac{\sqrt{b^2 + c^2 - 2bc \cos \theta_a}}{cb \sin \theta_a} \left[J_a \ddot{\theta}_a + B_a \dot{\theta}_a - m_a g l_m \cos(\theta_a + \phi) \right]. \quad (13)$$

Our position control approach first considers the problem of controlling θ_a given τ_a , assuming no gravity is present. The relation between τ_a and θ_a in this case is given as

$$\frac{\theta_a}{\tau_a} = \frac{1}{s^2 J_a + s B_a}. \quad (14)$$

Inverting (14) provides a desired arm torque ($\tau_{a,des}$) given a desired arm angle (θ_d) and is used as the initial block in the position controller (see Fig. 13). Because (14) does not consider gravity, the desired arm torque signal must be summed with a gravity compensation torque (12) to produce the expected motion. The resulting torque value is then converted into desired actuator force by multiplying by the inverse of the nonlinear kinematics [L^{-1} from (10)]. This desired force is then passed to the force controller.

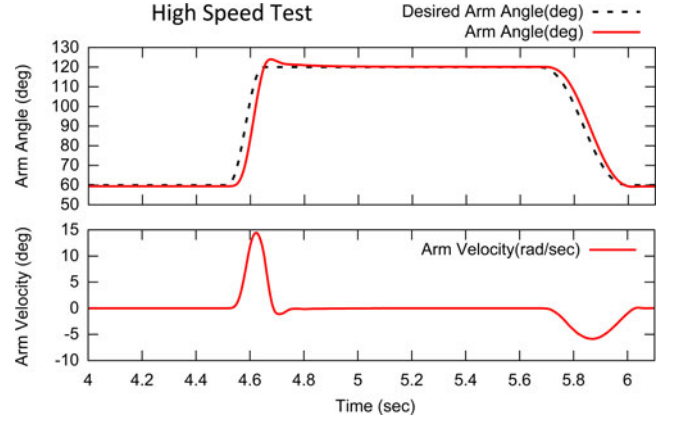


Fig. 14. High-speed position tracking test. The actuator output follows a reference signal that changes 60° in less than 0.2 s. The actuator is able to track the reference signal closely and reaches the maximum mechanical speed of the ball screw of 15 rad/s. The torque moment arm (L) rotates through its largest length at $\theta_a = 90^\circ$.

Without some form of feedback the position controller would not be able to track a desired position due to modeling error and external disturbances. A DOB is placed in an outer loop around the model-based position controller to resolve these issues. The DOB treats modeling error and exogenous input as a disturbance and counteracts this disturbance with input to the model-based position controller. Q_p ($f_c = 10$ Hz) in Fig. 13 is a feedforward low-pass filter to smooth position response, thus, reducing required torques. Q_{pd} ($f_c = 35$ Hz) is a low-pass filter that attenuates high-frequency disturbance signals of the DOB.

IV. PERFORMANCE EXPERIMENTS AND ENERGETICS

Our goal was to design hardware and controllers that would maximize actuator performance, but how do we know if we have been successful? One way of measuring the success of a control design is to attempt to reach the mechanical limits of an actuator's components in a safe and controlled manner. To this end, we performed an experiment to push actuator speed to the limits of its mechanical and control capability. A fifth-order spline was used to generate a smooth position reference signal for high-speed transitions between a large angle displacement (60°). Fig. 14 shows the experimental results. The arm is able to track the reference position closely and achieves a velocity of 15 rad/s which is the mechanical limit of the ball screw. In this test, the motor reached a speed of 22 600 r/min which is 3000 r/min below the maximum possible motor speed. Acceleration from rest, to maximum speed, and back to rest occurs within less than 0.2 s.

A critical actuator performance metric is power output. To maximize measured power output, we designed an experiment which would require high speed and high torque simultaneously. The design of the output arm to which the actuator is attached allows for additional weight to be added. For the experiment, we fixed a 4.5-kg weight to the arm with a 0.23-m moment arm. The experiment requires the arm to track a reference position which is again generated using splines. The motion is not symmetrical. When the weight is being lowered the reference signal changes

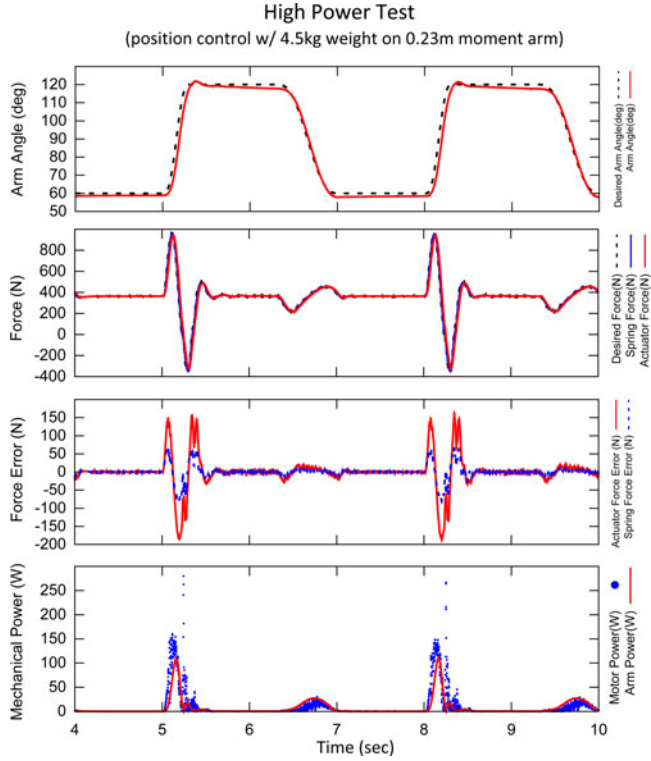


Fig. 15. Data from the high-power test. Accuracy of both position and force tracking can be seen in the top two graphs. The third graph shows force error of both spring force and output force (see Section III-A). The bottom graph shows power measured at the motor (desired torque time motor velocity) and at the output (measured torque times measured velocity). The following variable mappings are used: Desired Arm Angle (θ_d), Arm Angle (θ_a), Desired Force (F_d), Spring Force (F_k), Actuator Force ($F_{o_{est}}$).

slowly, and when the weight is being raised the reference signal changes quickly. The combination of fast motion and the fact that the motion is directed upwards against gravity makes this test require very high actuator power output. Fig. 15 shows the experimental results. On the bottom, graph power at the motor and power at the arm can be seen. The output power is measured as output torque times output velocity. The actuator generates peak mechanical output power of approximately 110 W, which corresponds to a power-to-weight ratio of 94 W/kg. Comparing with [4], this represents a 47% improvement over previous attempts. While these are strong results, we believe that the actuator is capable of much higher output. We plan to test this hypothesis in future design iterations.

The error during high acceleration shown in Fig. 15 may be attributed to the following factors. First, the high-output impedance model assumed for system identification does not consider motion of the load. Depending on the amount of tolerable error, this system identification model may be extended to include dynamics of the load side of the actuator, although it should be noted that doing so reduces the modularity of the actuation system in general and requires the control law to be tailored to load characteristics. Second, as depicted in Fig. 11, the UT-SEA is not able to track force accurately near its resonant frequency. Using an FSEA style actuator would improve

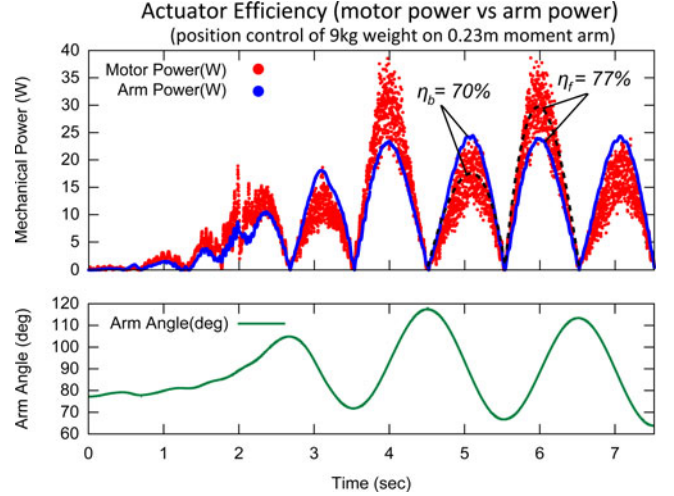


Fig. 16. Test to measure actuator mechanical efficiency. The arm is tracking a sinusoidal position reference with weight added. Motor power is calculated from desired motor torque times measured motor velocity, while arm power is calculated from measured arm torque times measured arm velocity. η_f and η_b represent forward and backward efficiency, respectively. On upward swings, motor power is greater than arm power because the actuator must work against gravity. On downward swings, arm power is greater than motor power due to gravity backdriving the actuator.

this aspect of force tracking at the cost of increased actuator size and weight, as discussed in Section II-C.

We present one final experiment aimed at measuring actuator efficiency. There are several places for loss to occur as energy is transferred through an actuation system. We designed an experiment to measure the efficiency of power transfer from the output of the motor to the output of the actuator. The experiment was performed by fixing a 9-kg weight to the arm and tracking a sinusoidal position reference and measuring power at each location. Fig. 16 shows the experimental results. Interestingly, peak arm power remains the same regardless of the direction of travel while motor power does not. This indicates that the transfer of power reverses direction depending on whether the arm is rising or falling. When the arm is rising, the motor is injecting power into the system, and there is a loss from the motor to the output. When the arm is falling, *gravity* is injecting power into the system and there is a loss in the opposite direction, from the output to the motor. The motor data are not as clean as the output data because the desired torque values are changing rapidly due to automatic control. To calculate efficiency, we fit a fourth-order curve to each phase of the motor data. Efficiency in the forward direction from the motor to the output (η_f) was measured to be 77%, while efficiency in the reverse direction (η_b) was 70%. This experiment does not consider the efficiency of converting the electrical power into the mechanical power of the motor. However, efficiency of the motor drive's H-bridge and the efficiency of the motor can be very high, mostly depending on motor load. We plan to measure this efficiency in future work.

Experiments were performed on a PC-104 form factor computer from Advanced Digital Logic (ADLS15PC) running Ubuntu Linux with an RTAI patched kernel to enable real-time computation. Data were passed to and from the actuator using analog and quadrature signals which pass through a custom

signal conditioning board. Both force and position control were performed at a servo frequency of 1 kHz. All continuous time control structures and signal time derivatives were converted to discrete time using a bilinear (Tustin) transform and were implemented in C.

V. CONCLUSION

This paper introduced the UT-SEA, a compact, lightweight, high-power actuator designed to empower the next generation of electrically actuated machines. Unlike other prismatic SEAs, the UT-SEA features a tightly integrated pushrod design which allows the actuator to be housed within a robotic limb and use a nonlinear mechanical linkage to drive a rotary joint. High motor voltage and current filtering enable the use of a large speed reduction which significantly increases both continuous and peak torque capabilities. Placement of the elastic element between the actuator housing and chassis ground creates a design with increased range of motion and small size.

We presented methods for modeling both the FSEA and RFSEA style actuators which revealed fundamental differences between the two in terms of the controller design and force tracking capability. Although RFSEA style actuators present difficulties, we proposed a control design based on model-based, PID, and DOB structures and validated the controller in hardware. The proposed force controller was able to track forces with 98.4% less error than conventional PD-based control for low-frequency signals and removed harmful spring resonance associated with RFSEA designs. We also presented a model-based position controller which includes the proposed force controller as the innermost loop. We performed high-speed tracking experiments with this controller and achieved speeds of 15 rad/s which is the mechanical limit of the hardware. Additional tests showed peak actuator power output of 110 W and mechanical efficiency of 77%.

ACKNOWLEDGMENT

The authors would like to thank members of the UT ME Machine Shop, especially S. Allen, for their valuable input during the design and fabrication phase. They would also like to thank A. Kwok for helping with spring support guide experiments.

REFERENCES

- [1] G. Pratt and M. Williamson, "Series elastic actuators," in *Proc. IEEE/RSJ Int. Conf. Intell. Robot. Syst. Human Robot Interact. Cooper. Robot.*, Aug. 1995, vol. 1, pp. 399–406.
- [2] S. Arumugom, S. Muthuraman, and V. Ponselvan, "Modeling and application of series elastic actuators for force control multi legged robots," *J. Comput.*, vol. 1, no. 1, pp. 26–33, Dec. 2009.
- [3] D. Paluska and H. Herr, "Series elasticity and actuator power output," in *Proc. IEEE Int. Conf. Robot. Autom.*, May 2006, pp. 1830–1833.
- [4] J. Pestana, R. Bobin, J. C. Arevalo, and E. Garcia Armada, "Characterization of emerging actuators for empowering legged robots," presented at the 13th Int. Conf. Climbing and Walking Robots Support Technologies Mobile Machines, Nagoya, Japan, 2010.
- [5] F. Parietti, G. Baud-Bovy, E. Gatti, R. Riener, L. Guzzella, and H. Vallery, "Series viscoelastic actuators can match human force perception," *IEEE/ASME Trans. Mechatronics*, vol. 16, no. 5, pp. 853–860, Oct. 2011.
- [6] S. Curran and D. Orin, "Evolution of a jump in an articulated leg with series-elastic actuation," in *Proc. IEEE Int. Conf. Robot. Autom.*, May 2008, pp. 352–358.
- [7] M. Hutter, C. Remy, and R. Siegwart, "Design of an articulated robotic leg with nonlinear series elastic actuation," in *Proc. 12th Int. Conf. Clim. Walking Robot. Supp. Technol. Mobile Mach.*, Sep. 2009, pp. 645–652.
- [8] K. Kong, J. Bae, and M. Tomizuka, "Control of rotary series elastic actuator for ideal force-mode actuation in human-robot interaction applications," *IEEE/ASME Trans. Mechatronics*, vol. 14, no. 1, pp. 105–118, Feb. 2009.
- [9] D. Ragonesi, S. Agrawal, W. Sample, and T. Rahman, "Series elastic actuator control of a powered exoskeleton," in *Proc. IEEE Annu. Int. Conf. Eng. Med. Biol. Soc.*, Sep. 2011, pp. 3515–3518.
- [10] C. Lagoda, A. Schouten, A. Stienen, E. Hekman, and H. van der Kooij, "Design of an electric series elastic actuated joint for robotic gait rehabilitation training," in *Proc. IEEE 3rd RAS and EMBS Int. Conf. Biomed. Robot. Biomechatron.*, Sep. 2010, pp. 21–26.
- [11] M. Diftler, J. Mehling, M. Abdallah, N. Radford, L. Bridgwater, A. Sanders, R. Askew, D. Linn, J. Yamokoski, F. Permenter, B. Hargrave, R. Piatt, R. Savely, and R. Ambrose, "Robonaut 2—The first humanoid robot in space," in *Proc. IEEE Int. Conf. Robot. Autom.*, May 2011, pp. 2178–2183.
- [12] M. Hutter, C. Remy, M. Hoepfner, and R. Siegwart, "ScarLETH: Design and control of a planar running robot," in *Proc. IEEE/RSJ Int. Conf. Intell. Robot. Syst.*, Sep. 2011, pp. 562–567.
- [13] E. Torres-Jara and J. Banks, "A simple and scalable force actuator," presented at the Int. Symp. Robot., Paris, France, Mar. 2004.
- [14] K. Kong, J. Bae, and M. Tomizuka, "A compact rotary series elastic actuator for human assistive systems," *IEEE/ASME Trans. Mechatronics*, vol. 17, no. 2, pp. 288–297, Apr. 2012.
- [15] M. D. Taylor, "A compact series elastic actuator for bipedal robots with human-like dynamic performance," Master's thesis, Robotics Inst., Carnegie Mellon Univ., Pittsburgh, PA, USA, 2011.
- [16] A. Edsinger-Gonzales and J. Weber, "Domo: A force sensing humanoid robot for manipulation research," in *Proc. IEEE/RAS 4th Int. Conf. Humanoid Robot.*, Nov. 2004, vol. 1, pp. 273–291.
- [17] P. Gregorio, M. Ahmadi, and M. Buehler, "Design, control, and energetics of an electrically actuated legged robot," *IEEE Trans. Syst., Man, Cybern. B, Cybern.*, vol. 27, no. 4, pp. 626–634, Aug. 1997.
- [18] J. Pratt and G. Pratt, "Intuitive control of a planar bipedal walking robot," in *Proc. IEEE Int. Conf. Robot. Autom.*, May 1998, vol. 3, pp. 2014–2021.
- [19] J. E. Pratt and B. T. Krupp, "Series elastic actuators for legged robots," in *Proc. SPIE 5422, Unmanned Ground Vehicle Technol. VI*, 2004, pp. 135–144.
- [20] J. Hurst, J. Chestnutt, and A. Rizzi, "The actuator with mechanically adjustable series compliance," *IEEE Trans. Robot.*, vol. 26, no. 4, pp. 597–606, Aug. 2010.
- [21] T.-H. Huang, J.-Y. Kuan, and H.-P. Huang, "Design of a new variable stiffness actuator and application for assistive exercise control," in *Proc. IEEE/RSJ Int. Conf. Intell. Robot. Syst.*, Sep. 2011, pp. 372–377.
- [22] N. G. Tsarakakis, I. Sardellitti, and D. G. Caldwell, "A new variable stiffness actuator (CompAct-VSA): Design and modelling," in *Proc. IEEE/RSJ Int. Conf. Intell. Robot. Syst.*, Sep. 2011, pp. 378–383.
- [23] M. Grebenstein, A. Albu-Schaffer, T. Bahl, M. Chalon, O. Eiberger, W. Friedl, R. Gruber, S. Haddadin, U. Hagn, R. Haslinger, H. Hoppner, S. Jorg, M. Nickl, A. Nothelfer, F. Petit, J. Reill, N. Seitz, T. Wimbock, S. Wolf, T. Wusthoff, and G. Hirzinger, "The DLR hand arm system," in *Proc. IEEE Int. Conf. Robot. Autom.*, May 2011, pp. 3175–3182.
- [24] A. Jafari, N. Tsarakakis, and D. Caldwell, "A novel intrinsically energy efficient actuator with adjustable stiffness (AwAS)," *IEEE/ASME Trans. Mechatronics*, vol. 18, no. 1, pp. 355–365, Feb. 2013.
- [25] I. Thorson and D. Caldwell, "A nonlinear series elastic actuator for highly dynamic motions," in *Proc. IEEE/RSJ Int. Conf. Intell. Robot. Syst.*, Sep. 2011, pp. 390–394.
- [26] K. Kong, J. Bae, and M. Tomizuka, "A compact rotary series elastic actuator for knee joint assistive system," in *Proc. IEEE Int. Conf. Robot. Autom.*, May 2010, pp. 2940–2945.
- [27] J. W. Sensinger and R. F. Weir, "Unconstrained impedance control using a compact series elastic actuator," in *Proc. IEEE/ASME 2nd Int. Conf. Mechatron. Embedd. Syst. Appl.*, Aug. 2006, pp. 1–6.
- [28] E. Garcia, J. Arevalo, F. Sanchez, J. Sarria, and P. Gonzalez-de Santos, "Design and development of a biomimetic leg using hybrid actuators," in *Proc. IEEE/RSJ Int. Conf. Intell. Robot. Syst.*, Sep. 2011, pp. 1507–1512.
- [29] G. Pratt, P. Willisson, C. Bolton, and A. Hofman, "Late motor processing in low-impedance robots: Impedance control of series-elastic actuators," in *Proc. Amer. Control Conf.*, Jul. 2004, vol. 4, pp. 3245–3251.
- [30] H. Vallery, R. Ekkelenkamp, H. van der Kooij, and M. Buss, "Passive and accurate torque control of series elastic actuators," in *Proc. IEEE/RSJ Int. Conf. Intell. Robot. Syst.*, Nov. 2007, pp. 3534–3538.

- [31] G. Wyeth, "Control issues for velocity sourced series elastic actuators," presented at the Australian Conf. Robot. Autom., Auckland, New Zealand, Dec. 2006.
- [32] M. Hutter, C. Remy, M. Hoepflinger, and R. Siegwart, "High compliant series elastic actuation for the robotic leg ScarLETH," presented at the Int. Conf. Climbing Walking Robots and the Support Technologies for Mobile Machines, Paris, France, 2011.
- [33] A. Beelen and A. J. Sargeant, "Effect of fatigue on maximal power output at different contraction velocities in humans," *J. Appl. Physiol.*, vol. 71, no. 6, pp. 2332–2337, 1991.
- [34] A. Zoss, H. Kazerooni, and A. Chu, "Biomechanical design of the berkeley lower extremity exoskeleton (BLEEX)," *IEEE/ASME Trans. Mechatronics*, vol. 11, no. 2, pp. 128–138, Apr. 2006.
- [35] P. Garrec, "Design of an anthropomorphic upper limb exoskeleton actuated by ball-screws and cables," *Proc. Sci. Bull. Ser. D*, vol. 72, no. 2, pp. 23–34, 2010.
- [36] O. Khatib, "A unified approach for motion and force control of robot manipulators: The operational space formulation," *IEEE J. Robot. Autom.*, vol. 3, no. 1, pp. 43–53, Feb. 1987.
- [37] J. Pratt, C.-M. Chew, A. Torres, P. Dilworth, and G. Pratt, "Virtual model control: An intuitive approach for bipedal locomotion," *Int. J. Robot. Res.*, vol. 20, no. 2, pp. 129–143, 2001.
- [38] N. Hogan, "Impedance control: An approach to manipulation," in *Proc. Amer. Control Conf.*, Jun. 1984, pp. 304–313.
- [39] H. S. Lee and M. Tomizuka, "Robust motion controller design for high-accuracy positioning systems," *IEEE Trans. Ind. Electron.*, vol. 43, no. 1, pp. 48–55, Feb. 1996.



Nicholas Paine (S'12) received the B.S. and M.S. degrees in electrical engineering from the University of Texas at Austin, Austin, TX, USA, in 2008 and 2010, respectively, where he is currently working toward the Ph.D. degree in electrical engineering.

His research interests include design and control of actuators and systems for dynamic legged robots.

Mr. Paine received the Virginia & Ernest Cockrell, Jr. Fellowship in Engineering in 2008.



Sehoon Oh (S'05–M'06) received the B.S., M.S., and Ph.D. degrees in electrical engineering from The University of Tokyo, Tokyo, Japan, in 1998, 2000, and 2005, respectively.

He was an Assistant Professor in the Department of Electrical Engineering at The University of Tokyo until 2012, and was a Visiting Researcher at the University of Texas at Austin from 2010 to 2011. He is currently a Research Professor at Sogang University, Seoul, Korea. His research interests include the development of human-friendly motion control algorithms and assistive devices for people.

Dr. Oh is a member of the Institute of Electrical Engineers of Japan.



Luis Sentis (S'04–M'07) received the M.S. and Ph.D. degrees in electrical engineering from Stanford University, Stanford, CA, USA, where he developed leading work in theoretical and computational methods for the compliant control of humanoid robots. Prior to that, he worked in Silicon Valley in the area of clean room automation.

He is currently an Assistant Professor at the University of Texas at Austin, Austin, TX, USA, where he directs the Human Centered Robotics Laboratory.

His research focuses on foundations for the compliant control of humanoid robots, algorithms to generate extreme dynamic locomotion, and building robots for educating students in mechatronics.